Organic Electronics 86 (2020) 105922

Contents lists available at ScienceDirect

Organic Electronics

journal homepage: http://www.elsevier.com/locate/orgel

Enhanced efficiency and reduced hysteresis by TiO_2 modification in high-performance perovskite solar cells

Veera Murugan Arivunithi [a], Soohyun Kim [b], Jungmin Choi [a], Jong Hun Sung [c], Hyun Deog Yoo [c], Eun-Sol Shin [d], Yong-Young Noh [d], Yeong-Soon Gal [e], Hyunjung Lee [b,**], Sung-Ho Jin [a,*]

[a] Department of Chemistry Education, Graduate Department of Chemical Materials, Institute for Plastic Information and Energy Materials, Pusan National University, Busan, 46241, Republic of Korea
[b] Department of Materials Science and Engineering, Kookmin University, Seoul, 02707, Republic of Korea
[c] Department of Chemistry and Chemical Institute for Functional Materials, Pusan National University, Busan, 46241, Republic of Korea
[d] Department of Chemical Engineering, Pohang University of Science and Technology (POSTECH), Pohang, 37673, Republic of Korea
[e] Department of Fire Safety, Kyungil University, Gyeongsan, 38428, Republic of Korea

ARTICLE INFO

Keywords:
4-Chlorobenzoic acid
Perovskite solar cell
Mesoporous TiO_2
Dopant
High efficiency
Stability

ABSTRACT

Recent research has focused on increasing the open-circuit voltage (V_{OC}) and current density (J_{SC}) of perovskite solar cells (PSCs) by introducing p- or n-type dopants with higher electronegativity than Ti into the TiO_2 electron transport layer (ETL). However, these kinds of dopant create undesired charge traps that hinder charge transport through TiO_2. Therefore, the improvement in V_{OC} is often accompanied by an undesired current density–voltage (J–V) hysteresis problem. Herein, we demonstrate that the introduction of 4-chlorobenzoic acid (4-ClBA-TiO_2) dopant into TiO_2 not only overcomes the J–V hysteresis issue but also increases the V_{OC}, J_{SC} and power conversion efficiency (PCE) in mesoscopic PSCs. Also, the material shown the better device performance compared to the state-of-art ETL, with the 4-CLBA-TiO_2. We speculate that the interaction between the 4-ClBA and the perovskite interface is more selective for electrons. Further the 4-ClBA-TiO_2 electron mobility has been improved 1.9 times compared with TiO_2. As a result, for mesoscopic PSCs, the doping of 4-ClBA-TiO_2 increases the efficiency from 18.23% to 20.22%, while the hysteresis is largely reduced from 20.2% to 1.5%. To the best of our knowledge, this is the first report using the spin coating blocking layer to achieve over 20%. Thus, we believe that this approach will be an effective design strategy capable of enhancing the performance of PSCs with less hysteresis.

1. Introduction

The development of perovskite solar cells (PSCs) with a sandwich configuration has shown a rapidly increased to 25.2%, which is "next big thing" in photovoltaics, as their power conversion efficiencies (PCE) were improved in a past decades [1–7]. A mesoporous titanium dioxide (TiO_2) layer on an FTO (F-doped SnO_2) surface serves as the photoanode of the device. The light absorption layer i.e., the, perovskite material is then layered and covered with a hole transport material (HTM). Finally, a metal counter electrode (Al, Ag or Au) to finish the device [8]. TiO_2 is the dominant electron transporting material to extract and transport photogenerated electrons and to prevent contact between the FTO and hole transport layer (HTL) [9]. Extensive research has been performed on HTMs and their importance as an interfacial layer in PSCs was also studied [10–12]. Although, the electron transport/selective layer (ETL) plays a significant role in enhancing the PCE and reducing the hysteresis effect, study on the bottom electrode is limited [13,14]. The most commonly used ETL is mesoporous TiO_2 nanoparticles. This TiO_2 nanoparticles are susceptible to intrinsic defects that cause low conductivity with poor charge conductance and form undesirable charge traps [15]. The various processing methods being researched is attributed to its role in improving the PSCs performance. Wu et al. studied the performance of PSCs by using different methods for fabricating the TiO_2 layer. They reported that TiO_2 fabricated using atomic layer deposition method (ALDM) exhibited higher shunt resistance and significantly improved the energy conversion efficiency due to the reduced density of

* Corresponding author.
** Corresponding author.
E-mail addresses: hyunjung@kookmin.ac.kr (H. Lee), shjin@pusan.ac.kr (S.-H. Jin).

https://doi.org/10.1016/j.orgel.2020.105922
Received 17 April 2020; Received in revised form 30 July 2020; Accepted 5 August 2020
Available online 14 August 2020

nanoscale pinholes in the layer. They also demonstrated that the fabricated devices using ALDM and spray pyrolysis result in higher conversion efficiencies. Researchers have been attempting to improve the charge conductivity and reduce the series resistance through doping TiO_2 with metals, C_{60} derivatives, inorganic materials, polymer, and small molecular materials [16]. Doping of lithium (Li) TiO_2 improved the V_{OC} when the Li dopant passivates electronically defect states. V_{OC} of the PSCs can be enhanced by removing the recombination centers related to the charge traps in TiO_2. The vital challenge in PSCs are hysteresis effect [17], which means the *J–V* curves vary with different scan directions. The origin of hysteresis is still being investigated in PSCs [13]. Also, interface modification between the perovskite layer and metallic oxide has been researched as a strategy for the high performance of PSCs by control of interfacial charge transport [18–21]. Among the modification materials, benzoic acid derivatives have been considered as effective materials because of its high electron affinity by the substituted group resulted in reduced charge recombination and enhanced electron extraction from perovskite to electron transport layers [16,22]. Benzoic acid has already been used in the surface modification properties in inorganic semiconductors other than TiO_2. It has been successfully utilized in dye-sensitized solar cells and organic solar cells [23–26]. The chloro-substituent, as one of benzoic acid derivatives, has a high value (3.16) of the electronegativity [26]. Herein, we introduce 4-chlorobenzoic acid (4-ClBA), having the high electron-withdrawing ability by high electro negativity of chloro-substituent as one of benzoic acid derivatives, into mesoporous TiO_2. The synthesized 4-ClBA-TiO_2 was successfully utilized in PSCs and their performance as ETL was evaluated. As a result, the efficiency was increased from 18.23% to 20.22% for mesoscopic PSCs, while the percentage of hysteresis was reduced from 20.2% to 1.5% by doping 4-ClBA into TiO_2.

2. Results and discussion

The synthesizing scheme of 4-ClBA-TiO_2 is shown in Fig. 1. The synthesized 4-ClBA-TiO_2 was confirmed by X-ray diffraction (XRD), Fourier transform infrared (FT-IR) spectroscopy and scanning electron microscopy (SEM) analysis. Fig. 2a–b shows FT-IR peaks at 1530–1545 cm^{-1} and 1407–1409 cm^{-1}, which newly represent formed asymmetric and symmetric carboxylate groups (COO-). The disappearance of the peaks at 1677 cm^{-1} (C═O) and 1283 cm^{-1} (C–OH) confirmed the absence of residual 4-ClBA. It means that 4-ClBA was absorbed on TiO_2 surface with bidentate interaction through dissociation carboxyl group [27–29]. The XRD spectra confirmed that no changes were observed in the crystal structure (Fig. 2c). The effect of 4-ClBA doping was characterized using SEM to check the particle aggregation and size variation in Fig. 3. Synthesized TiO_2 (Fig. 3a) indicated uniform size (48 ± 9 nm). After 4-ClBA doping, the 4-ClBA-TiO_2 particles retained the uniform size (49 ± 5 nm) after the synthesis. Additionally, we observed hydrophobic property in its surface in TiO2 due to 4-ClBA doping. The changes in surface properties were confirmed by dispersing the surface modified particles into chlorobenzene (CB) as shown in Fig. S1. The TiO_2 nanoparticles synthesized by the hydrothermal method showed hydrophilicity and were well dispersed in DIW while not being dispersed in CB. On the other hand, by the transition from hydrophilic to hydrophobic surface after adsorption of 4-ClBA on the TiO_2 nanoparticles, it showed excellent dispersibility in CB. Moreover, when the dispersion was confirmed after 20 h, the surface modified 4-ClBA-TiO_2 particles in THF showed improved dispersion compared to toluene. Because the synthesized TiO_2 in aqueous solvent was not dispersed (in) toluene as non-polar organic solvent, the THF as a polar aprotic solvent provided effective in the interaction between 4-ClBA and TiO_2. Therefore, 4-ClBA-TiO_2 particles modified in the THF were used for investigation of the performance in the PSCs. The film state of the synthesized 4-ClBA--doped TiO_2 was analyzed using atomic force microscopy (AFM) and field emission scanning electron microscopy (FE-SEM) study. The AFM images of the TiO_2 and 4-ClBA-TiO_2 films are shown in (Fig. 4a–b). The surface morphology according to film thicknesses were analyzed using AFM and the topography was analyzed using FE-SEM images (Fig. 4c–d) (low and high magnification) of the TiO_2 and 4-ClBA-doped TiO_2 films. The AFM and FE-SEM images predominantly showed uniform topographic perovskite films for TiO_2 and 4-ClBA-doped TiO_2. The 4-ClBA-TiO_2 films showed relatively better morphology than that of TiO_2. The FE-SEM of TiO_2 film and perovskite layer deposited on TiO_2 three-dimension AFM images are presented in Fig. S2.

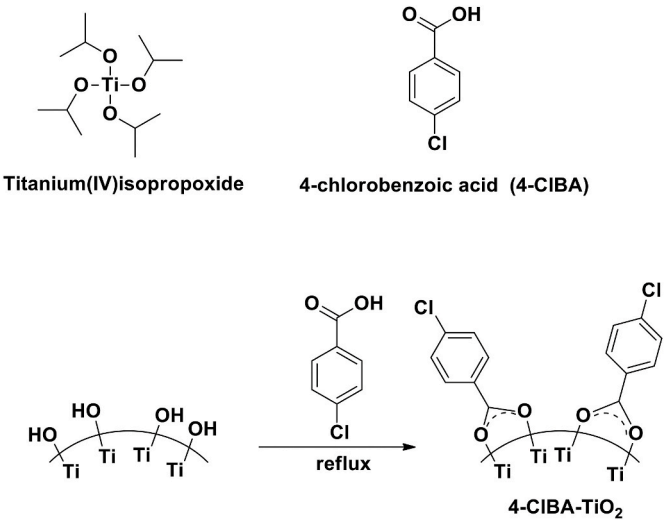

Fig. 1. Synthesizing scheme of 4-ClBA-TiO_2.

The chemical composition of the TiO_2 and 4-ClBA-TiO_2 films with FTO was analyzed by energy dispersive X-ray spectroscopy (EDS) in the binding region of 0–20 KeV, as shown in Fig. S3. The Sn and Si peaks were attributed to FTO, while the Ti and O peaks to TiO_2. Due to the low 4-ClBA concentration the percentage of the dopant was less than 1%. The bandgap (E_g), calculated from the UV–vis onset absorption, was reduced by 4-ClBA doping from 3.56 eV (TiO_2) to 3.50 eV (4-ClBA-TiO_2) (Fig. S4).The impact of 4-ClBA-doping on TiO_2 was evaluated by XRD, X-ray photoelectron spectroscopy (XPS) and ultraviolet photoelectron spectroscopy (UPS) studies (Fig. 5). Fig. 5a represents the TiO_2 and 4-ClBA-doped TiO_2 XRD spectra of the film. It clearly shows that there were no any impurity peaks were observed. We performed XPS analysis to gain information on the surface chemical deposition of TiO_2 and 4-ClBA-doped TiO_2. The survey spectra of pure and 4-ClBA doped TiO_2 is shown in Fig. 5b confirms the phase of pure TiO_2 by obtaining the Ti and O peaks at corresponding binding energies. As shown in Fig. 5b–c, no peaks were observed, possibly due to the low concentration of 4-ClBA doping. The peak shift appearing at 559 eV for Ti $2p_{3/2}$ further confirms the doping of 4Cl-BA in TiO_2. Also, we performed UPS analysis to confirm the result of 4-ClBA modification on its energy level of TiO_2 (Fig. 5d). A slight variation was detected in the high binding energy edge upon the modification of 4-ClBA-doped TiO_2. Fig. 5d shows that the doping of 4-CIBA upshifted the band edges by measuring photoemission cutoff in the secondary cutoff region. In addition to the chemical modification shown in Fig. S5, the band structure change was observed in 4-ClBA-TiO_2, upshifting the valence band (VB) edge of TiO_2 from 3.52 eV for TiO_2 to 3.49 eV for 4-ClBA-TiO_2.

The PSCs were fabricated with a configuration of FTO/TiO_2 (or) 4-ClBA-doped-TiO_2/Perovskite/2,2′,7,7′-tetrakis(*N*,*N*-di-*p*-methoxyphenylamine)-9,9′-spirobifluorene (Spiro-OMeTAD)/Au (Fig. 6). The energy band diagram and the schematic charge extraction process has been shown in Fig. S6. The fabrication condition of the PSCs is explained in detailed below. Fig. 6c and Fig. S7 shows the typical *J–V* curves of the reference cell and the optimized one using 4-ClBA-TiO_2 measured in both forward and reverse scan directions, respectively. The parameters

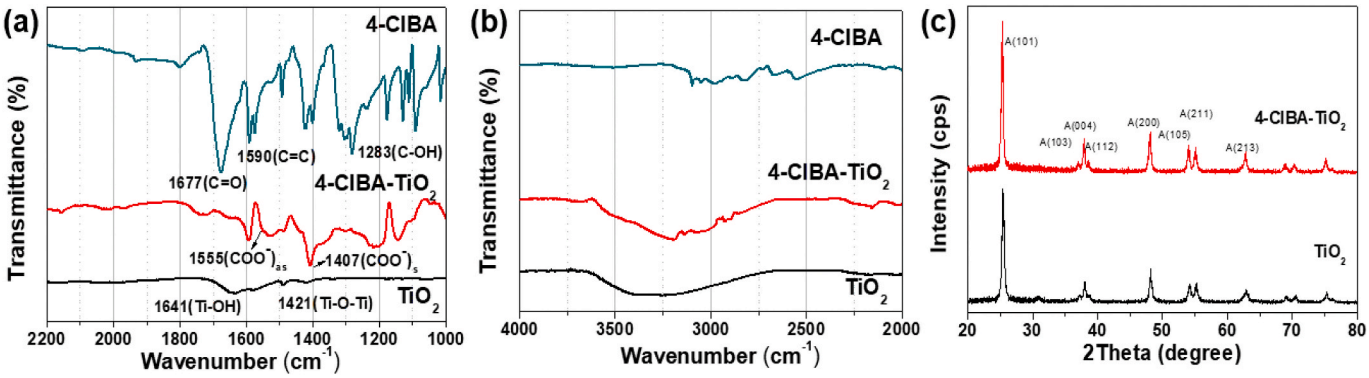

Fig. 2. a-b) FT-IR spectra TiO_2, 4-ClBA-TiO_2, and ClBA and c) XRD spectra of TiO_2 and synthesized 4-ClBA-TiO_2.

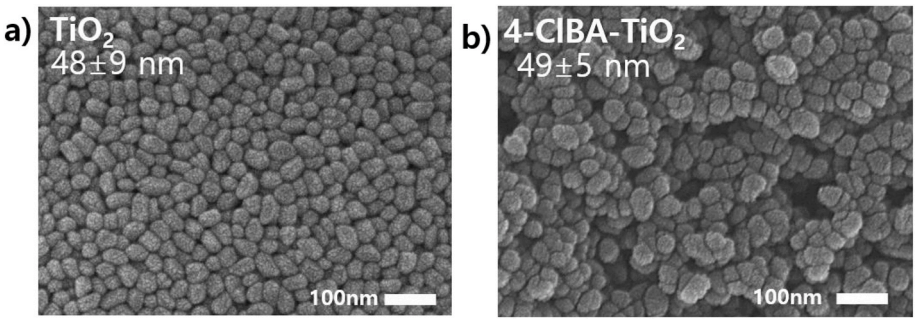

Fig. 3. SEM images and particle size of synthesized a) TiO_2 and **b)** 4-ClBA-TiO_2 modified in THF.

are shown in Table 1. A PCE of 18.23%, V_{OC} of 1.09 V, J_{SC} of 23.2 mA cm^{-2} and fill factor (FF) of 72.0% were achieved for the non-doped TiO_2. Remarkably, the introduction of 4-ClBA dopant into TiO_2 for use as the ETL in PSC devices further increased the PCE to 20.22%. At 0.05% doping, V_{OC}, J_{SC} and FF were increased to 1.12 V, 23.6 mA cm^{-2} and 76.4%, respectively. The substantial increases in both J_{SC} and FF were attributed to the large and higher quality of perovskite grains formed by doping. It is thus deduced that an extra electron-withdrawing group in the 4-ClBA will have a positive influence on the cell performance whereas electron-donating group might have negative impact to charge transport property, resulting in different effects on cell performance [16]. Thus, the charge recombination was efficiently suppressed and increased in the device performance.

Fig. 6d shows the external quantum efficiencies (EQEs) of the fabricated PSCs corresponding to AM1.5G illumination at an intensity of 100 mW cm^{-2}. The attributed integrated J_{SC} values of the TiO_2 and 4-ClBA-TiO_2 optimized devices were 22.8 and 22.7 mA cm^{-2}, which are well accorded with the *J–V* measurements. The hysteresis index (HI) was used to quantify the hysteresis loss observed from the measurement of the devices [30]. The hysteresis behavior of the PSCs using both the reverse and forward scan directions of TiO_2 and 4-ClBA-TiO_2 are shown in Fig. 6c. The HI of the devices is defined as follows;

$$HI = \frac{PCE_{Reverse} - PCE_{Forward}}{PCE_{Reverse}}$$

The calculated HI for PSCs with 4-ClBA-TiO_2 (0.013) was lower than that of pristine TiO_2 (0.05). The 4-ClBA-TiO_2 devices showed much lower (almost negligible) hysteresis than the non-doped ones. The hysteresis problem for doping metal remains unresolved due to the upward shift in the band structure of TiO_2. The higher HI of the pristine TiO_2-based PSCs clearly demonstrates great hysteresis, which explains the higher loss compared to the lower HI with visually indistinct hysteresis of doped PSCs in the *J-V* curves. Hysteresis is observed in electronic devices, particularly defect-rich, organic-based electronic devices, which contain a non-negligible amount of charge traps [31–33]. 4-ClBA passivate the traps on the TiO_2, resulting in a smoother surface, as observed in AFM; 4-ClBA doping improved the charge transportation at TiO_2/perovskite interface and has superior charge carrier extraction with better charge balance as illustrated in Fig. S6b. The efficient charge extraction and transportation resulted in the accumulation of charge at the interface and thereby reduce the hysteresis in 4-ClBA-TiO_2 PSCs [34]. Further, the reproducibility was confirmed by fabricating 15 devices with same procedure and *J–V* parameters, i.e., V_{OC}, J_{SC}, FF, and PCE's statistical distribution, are shown in Fig. 7. These key parameters show close distributions, which demonstrates the high reproducibility of the device fabrication. The device performance with spray pyrolysis and spin coated blocking TiO_2 layer compared with the previous reported is shown in (Table S1).

TiO_2 and 4-ClBA-TiO_2 were also evaluated by UV–vis absorption spectroscopy, electrochemical impedance spectroscopy (EIS), space charge limited current (SCLC) characteristics, current mobility of the electron only device (EOD), steady-state PL, and time-resolved PL (Fig. 8). UV–vis absorption spectra (Fig. 8a) of the films were relatively higher than those of the 4-ClBA-doped TiO_2/perovskite films, which confirmed that the absorption properties were increased due to the increased absorption of perovskite. To further understand the interfacial interaction of TiO_2 and 4-ClBA-TiO_2 [35], we measured the EIS for the fabricated devices under dark condition with an applied voltage equivalent to that of V_{OC}. Fig. 8b depicts the Nyquist plots for PSCs with both TiO_2 and 4-ClBA-TiO_2 layers. The Nyquist plots show that the recombination resistance for 4-ClBA-TiO_2 is larger than that of TiO_2--based films. The equivalent circuit model used to fit is also depicted in Fig. 8b (inset). The parameters were calculated using the equivalent circuit model and are tabulated in Table 2. The R_{rec} of the TiO_2 and 4-ClBA-TiO_2 optimized devices were calculated to be 545 and 2223 Ω, respectively. The larger R_{rec} value 4-ClBA-TiO_2 indicated a lower recombination loss, which evidenced the effective suppression for 4-ClBA-TiO_2 and the decreased traps in the interfaces. We fabricated

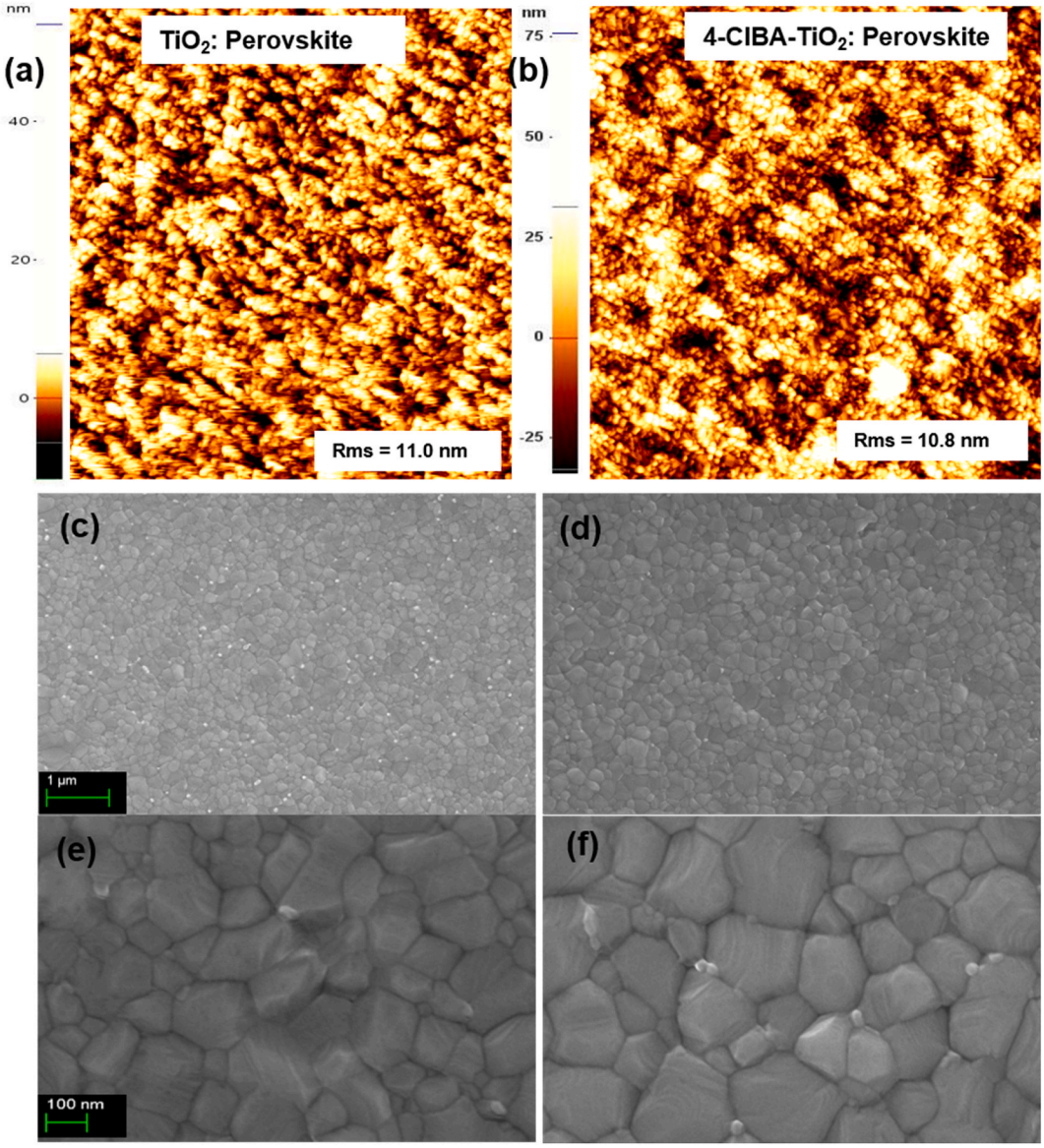

Fig. 4. Morphology of the TiO_2, and 4-ClBA-TiO_2 a-b) AFM images, c-d) low and e-f) high magnification FE-SEM images of perovskite.

EODs with device configuration of FTO (600 nm)/TiO_2 (180 nm)/Au (100 nm) to measure the mobility of TiO_2 and 4-ClBA-TiO_2 [16]. The mobilities were calculated by fitting the current to the model of the single carrier SCLC method. The *J-V* plots for EOD are shown in Fig. 8c and the inset shows the device structure of EOD. To calculate the mobility, we used the Mott–Gurney law as follows:

$$J = \left(\frac{9}{8}\right)\mu\varepsilon_o\varepsilon_r\left[\frac{V^2}{L^3}\right]$$

where μ, ε_o, ε_r, V, and L are the electron mobility, free space permittivity, dielectric constant, applied voltage, and thickness of the ETL film, respectively. The electron mobility calculated was increased 1.9 times from 2.7×10^{-5} for TiO_2 to 5.1×10^{-5} $cm^2\ V^{-1}\ s^{-1}$ for 4-ClBA-doped TiO_2. The high mobility was greatly influenced by the charge transport properties of 4-ClBA-TiO_2 [36].

Remarkably, the steady-state PL shows a clear decrease in absolute PL intensity in the following order: FTO > TiO_2 (or) 4-ClBA-TiO_2 > Perovskite (Fig. 8d). This confirmed that the doping of 4-ClBA was effective in the trap states of TiO_2 film. Time-resolved PL was carried out to understand the charge carrier kinetics properties of TiO_2 and 4-ClBA-doped TiO_2. Additionally, 4-ClBA-TiO_2 perovskite films (Fig. 8e) time-resolved PL with bi-exponential decay function shows a longer charge carrier lifetime than that of the TiO_2 perovskite films. The shortest PL lifetime, corresponding to 4.8 and 7.7 ns for 4-ClBA-TiO_2 and TiO_2, respectively. Thus, the 4-ClBA doped TiO_2 charge carriers were separated and transferred more effectively by stronger charge extracting ability with high electronegativity of chloro-substituent, which well aligned with the enhanced overall performance of the PSCs. These results are consistent with those of the steady-state measurements.

Since stability is one of the critical factors for commercialization, we investigated the stability of the fabricated optimized devices for the 4-ClBA-TiO_2 PSCs without any encapsulation (temperature: 25° ± 2, humidity: 30–40%), in comparison with the non-doped TiO_2 as reference. Degradation depends on the decomposition of the perovskite layer in atmosphere [37]. As shown in Fig. 8f, 4-ClBA-TiO_2 and TiO_2 exhibited similar deterioration performance.

3. Conclusions

In conclusion, properties such as light absorption, XRD measurement and SEM analyses revealed the negligible influence of 4-ClBA TiO_2 on

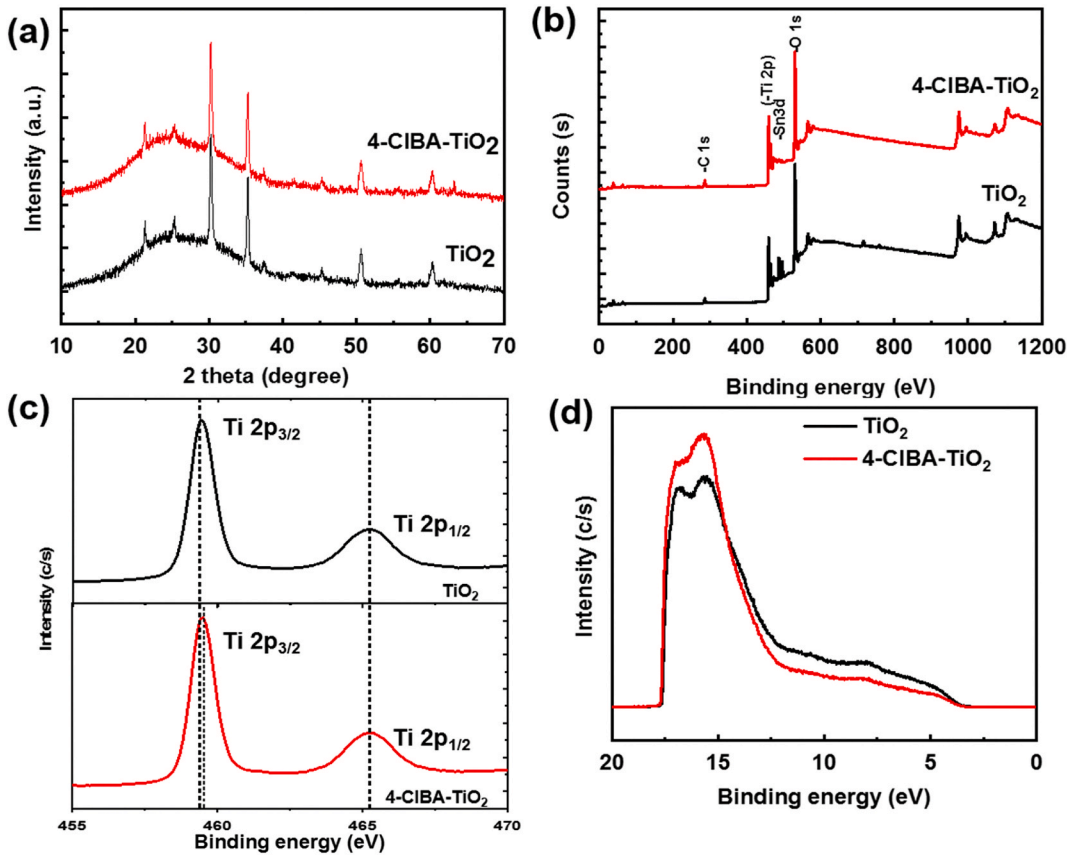

Fig. 5. a) XRD patterns, b-c) XPS spectra, and c) UPS spectra of TiO_2 and 4-ClBA-TiO_2 film.

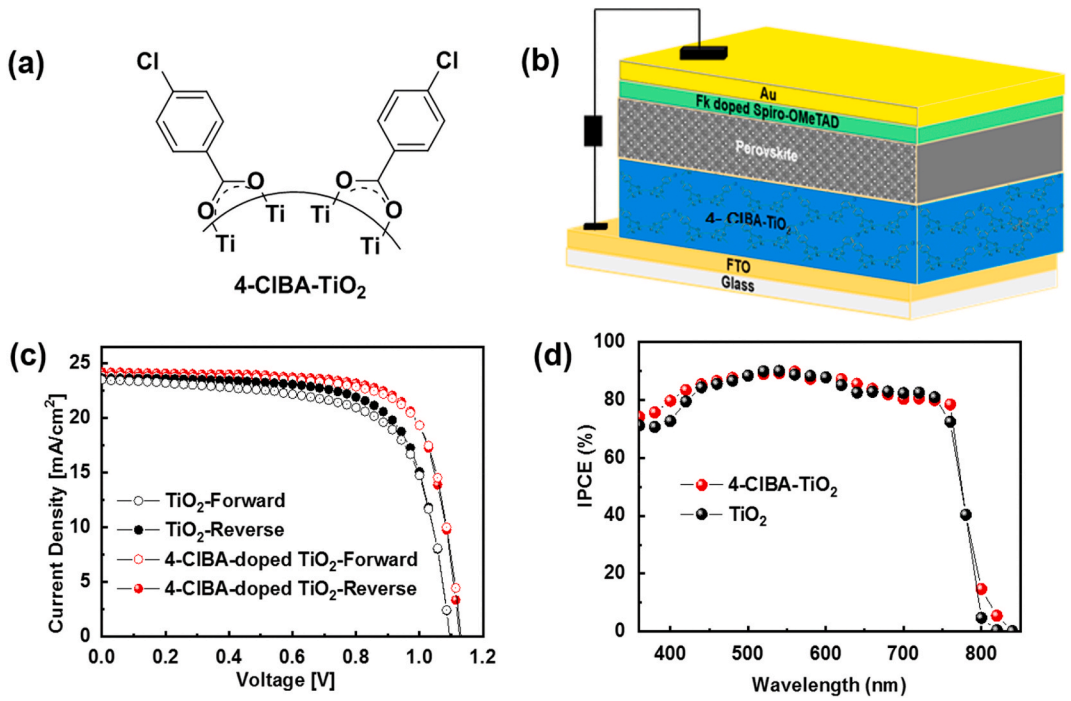

Fig. 6. a) Structure of 4-ClBA-TiO_2, b) the device structure of perovskite solar cell, c) *J–V* hysteresis behavior and d) EQEs with AM 1.5 G photon flux TiO_2, and 4-ClBA-TiO_2.

the perovskite film thickness, crystal structure, surface morphology and optical property. Also, the charge extracting ability of TiO_2 was enhanced after 4-ClBA doping by high electronegativity of chloro-substituent, as confirmed by transient PL spectra indicates high electron withdrawing ability resulted in effective charge extraction from perovskite to electron transport layers. In addition, 4-ClBA effectively

Table 1
Key *J-V* parameters measured for TiO_2 and 4-ClBA-TiO_2.

Device	J_{SC} (mA cm^{-2})	V_{OC} (V)	FF (%)	η (%)
TiO_2 (Reverse)	23.2	1.09	72.0	18.23
TiO_2 (Forward)	23.1	1.09	69.1	17.3
4-ClBA-TiO_2 (Reverse)	23.6	1.12	76.4	20.22
4-ClBA-TiO_2 (Forward)	23.4	1.12	76.1	19.94

passivated the traps on the TiO_2 surface. SEM analysis of 4-ClBA-doped TiO_2 shows better morphology with the particles in aggregation of synthesis. These results demonstrate the significant enhancement of the PSC device performance with 4-ClBA-TiO_2 due to the 1.9-fold increase in its mobility compared to TiO_2 with lower recombination resistance and fewer trap states. Conspicuously, the PCE of the PSCs with 4-ClBA-TiO_2 was dramatically improved from 18.23% to a maximum of 20.22% with negligible hysteresis. To summarize, the improvements offered by 4-ClBA doping support the potential for the commercialization of efficient PSCs.

3.1. Experimental section

Materials: Lead(II) iodide (PbI2) and lead(II) bromide (PbBr2) (99.99%) were purchased from TCI. Formamidinium iodide (FAI) and methylamine bromide (MABr) were purchased from Dyesol. Titanium diisopropoxide dis(acetylacetonate) was purchased from Sigma Aldrich (Korea). Spiro-OMeTAD (99.5%) was obtained from Lumtec (Taiwan). Acetonitrile (99.8%), chlorobenzene (CB, 99.8%), DMF (99.8%) and DMSO (99.9%) were purchased from Sigma Aldrich (Korea). For synthesis of 4-ClBA-TiO_2 nanoparticles, titanium(IV) isopropoxide (TTIP, 97%) was purchased from Sigma Aldrich (Korea). Tetramethylammonium hydroxide (TMAH, 25% in H2O) and 4-chloro benzoic acid (4-ClBA, >99.0%) was purchased from TCI. Tetrahydrofuran (THF, >99.0%) was purchased from Daejung Chemicals & Metals Co. (Korea). For preparation of 4-ClBA-TiO_2 paste, terpineol (≥95.0%) was purchased from Kanto Chemical Co. Ethyl cellulose (48.0–49.5% ethoxyl) was purchased from Sigma Aldrich (Korea). Lauric acid (>99.0%) was purchased from Daejung Chemicals & Metals Co. (Korea).

3.2. Synthesis of 4-ClBA-TiO_2 nanoparticles

TiO_2 nanoparticles were synthesized by hydrothermal process. TTIP as a TiO_2 precursor was dropped into deionized water (DIW) (0.18 M). TiO_2 particles were obtained through hydrolysis and condensation reaction with H_2O. The sediment was collected and washed by centrifugation with DIW (3000 rpm, 15mins). After peptization process in TMAH solution (0.15 M in H2O) at 85 °C for 24hrs, TiO_2 nanoparticles were synthesized by hydrothermal process at 200 °C for 10hrs. For surface modification of the TiO_2 nanoparticles with 4-ClBA, TiO_2 nanoparticles were collected by centrifugation followed drying in vacuum at 80 °C for 12hrs. The obtained particles were refluxed with 4-ClBA in THF (TiO_2:4-ClBA = 1:0.2, 0.4, 0.8 (w/w)) for 24hrs. 4-ClBA-TiO_2 paste was prepared by mixing with terpineol, ethyl cellulose and lauric acid in ethanol (TiO_2: terpineol: ethyl cellulose: lauric acid = 1.25 : 6: 0.6 : 1 (w/w)). After stirring of the mixture, ethanol was evaporated by rotary evaporator at 70 °C for 30min.

3.3. Fabrication of PSCs

Fluorine-doped tin oxide (FTO) glasses (Pilkington, TEC-8, 15Ω/sq) were etched using zinc powder and HCl solution (2 M). After cleaning by detergent, diluted water, and acetone, they were sonicated with isopropyl alcohol (IPA) in an ultrasonic bath for 60 min, followed by UV-O_3 treatment for 20 min. A 30 nm blocking TiO_2 (Bl-TiO_2) layer (0.15 M titanium diisopropoxide dis(acetylacetonate) with 1-butanol) was deposited on top of the FTO by spin coating TiO_2 precursor solution at

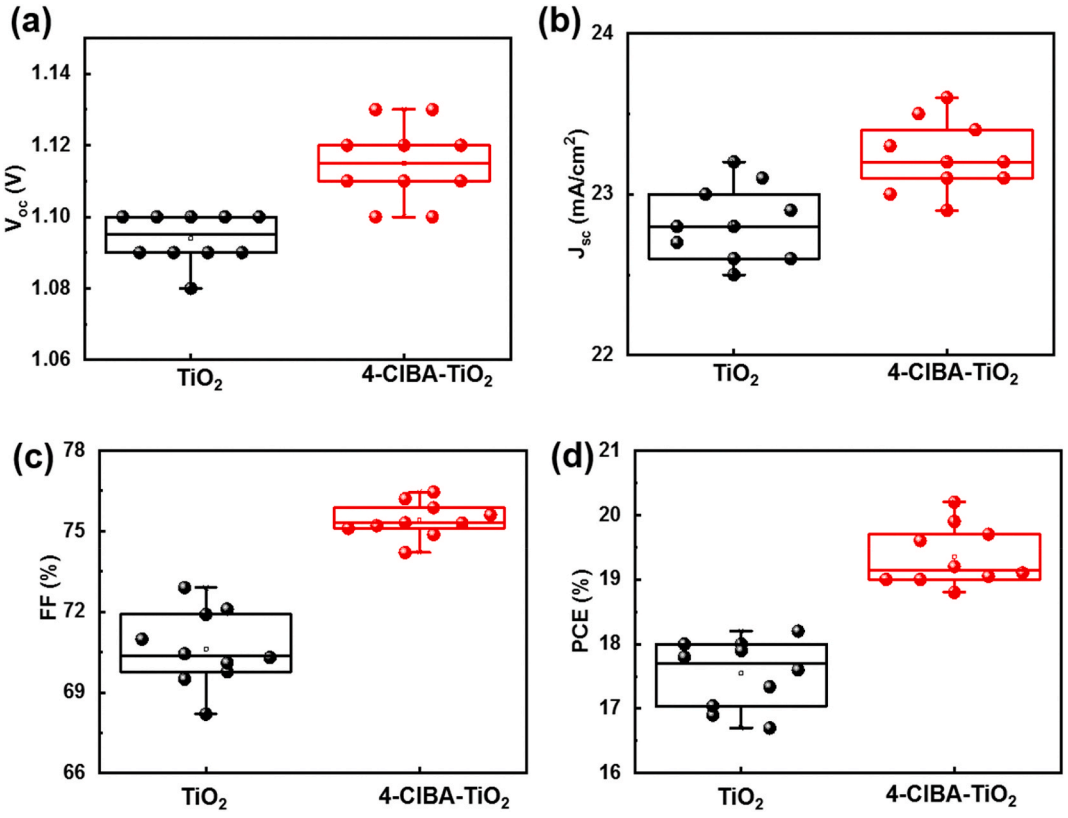

Fig. 7. Photovoltaic parameters of (a) open-circuit voltage (V_{OC}), (b) short-circuit current density (J_{SC}), (c) fill factor (FF), and (d) power conversion efficiency (PCE) of TiO_2 and 4-ClBA-TiO_2.

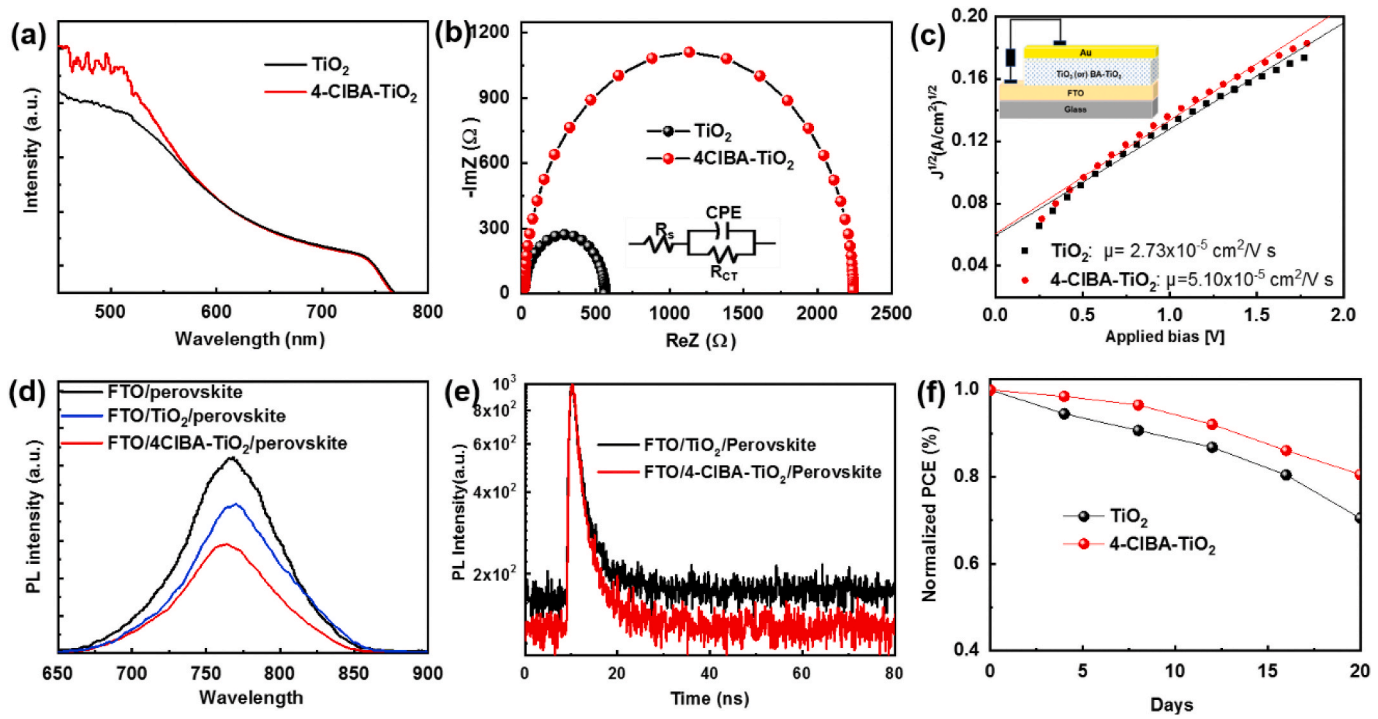

Fig. 8. a) Absorption spectra, b) impedance spectra, c) $J^{1/2}$–V curves for the SCLC electron mobility measurements and a schematic of the device structure for the SCLC measurements (inset), d) steady-state PL spectra, e) TRPL spectra and f) stability of TiO_2 and 4-ClBA-TiO_2.

Table 2
EIS parameters based on TiO_2 and 4-ClBA-TiO_2.

Device	R_s(Ω)	R_{rec} (Ω)	C_{rec} (F)
TiO_2	17.18	545	5.8×10^{-9}
4-ClBA-TiO_2	18.41	2223	5.6×10^{-9}

2800 rpm for 30 s. Next, it was heated at 125 °C for 5 min in air. The mesoporous titanium oxide (m-TiO_2) (or) 4-ClBA-TiO_2 layer was coated on Bl-TiO_2 substrates at 2000 rpm for 20 s to achieve 150–200 nm thickness using a diluted TiO_2 paste with ethanol and annealed at 600 °C for 1 h. The perovskite solution was prepared by dissolving 0.507 g of PbI_2, 0.080 g of $PbBr_2$, 0.022 g of MABr, and 0.171 g of FAI in 0.8 mL of anhydrous DMF and 0.2 mL of anhydrous DMSO. CsI (1.5 M in DMSO) was added to give a 5 vol% solution concentration. The spin coating procedure was performed in a glove box with nitrogen flow. Perovskite precursor solution was spin coated on the substrate at 1000 rpm for 10 s, and 4000 rpm for 20s. 200 μL of CB was injected on the substrate 10 s prior to the finish and then crystallized at 100 °C for 60 min in the glove box. Spiro-OMeTAD solution (35.0×10^{-3} M LiTFSI, 231×10^{-3} M tBP, 2.42×10^{-3} FK209) was spin coated at 5000 rpm for 30 s. Finally, a 100 nm gold electrode was vacuum deposited on the spiro-OMeTAD over layer.

3.4. Device characterizations

The film surface morphology was characterized by FE-SEM (HITACHI S-4800 field emission scanning electron microscope) and AFM images were acquired with an XE-100 (Park System Corp.) in tapping mode. The PL spectra were recorded with Hitachi F-4500 fluorescence spectrophotometers at room temperature. The samples were excited by a pulsed laser with a wavelength of 470 nm. The *J-V* curves were measured (Oriel® Sol3A™ Class AAA solar simulator, models 94043A) at 25 °C under AM1.5G (100 mW cm^{-2}) illumination using both forward (from I_{SC} to V_{OC}) and reverse (from V_{OC} to I_{SC}) scan modes adjusted using a standard PV reference cell (2 cm × 2 cm monocrystalline silicon solar cell, calibrated at NREL, Colorado, USA) and a computer controlled Keithley 2400 source measure unit. The incident photon-to-current conversion efficiency spectrum was measured using Oriel® IQE-200™ equipped with a 250 W quartz tungsten halogen lamp as the light source and a monochromator, an optical chopper, a lock-in amplifier, and a calibrated silicon photodetector. Prior to the illumination, the spectral response and light intensity were calibrated using a monosilicon detector. The impedance response was measured over the range of 1 Hz to 1 MHz with an oscillation amplitude of 15 mV under dark condition (Bio-Logic VMP-3). The experimental data were simulated using commercial Z-view software to estimate the values for each component of the corresponding equivalent circuits.

CRediT authorship contribution statement

Veera Murugan Arivunithi: Conceptualization, Methodology, Formal analysis, Writing - original draft, Writing - review & editing, Visualization. **Soohyun Kim:** Methodology, Formal analysis, Writing - original draft, Writing - review & editing, Visualization. **Jungmin Choi:** Formal analysis, Data curation. **Jong Hun Sung:** Visualization, Investigation. **Hyun Deog Yoo:** Formal analysis, Data curation. **Eun-Sol Shin:** Formal analysis, Data curation. **Yong-Young Noh:** Writing - review & editing. **Yeong-Soon Gal:** Formal analysis, Data curation. **Hyunjung Lee:** Writing - review & editing, Supervision, Project administration. **Sung-Ho Jin:** Writing - review & editing, Supervision, Project administration, Funding acquisition.

Declaration of competing interest

The authors declare that they have no known competing financial interests or personal relationships that could have appeared to influence the work reported in this paper.

Acknowledgements

V.M.A. and S.K. contributed equally to this work. This work was

supported by the National Research Foundation (NRF-2018R1A5A1025594) of the Ministry of Science and ICT.

Appendix A. Supplementary data

Supplementary data to this article can be found online at https://doi.org/10.1016/j.orgel.2020.105922.

References

[1] a) F. Hao, C.C. Stoumpos, D.H. Cao, R.P.H. Chang, M.G. Kanatzidis, Lead-free solid-state organic–inorganic halide perovskite solar cells, Nat. Photon. 8 (2014) 489;
b) J.-P. Correa-Baena, A. Abate, M. Saliba, W. Tress, T. Jesper Jacobsson, M. Gratzel, A. Hagfeldt, The rapid evolution of highly efficient perovskite solar cells, Energy Environ. Sci. 10 (2017) 710.

[2] H. Zhou, Q. Chen, G. Li, S. Luo, T.B. Song, H.S. Duan, Z. Hong, J. You, Y. Liu, Y. Yang, Interface engineering of highly efficient perovskite solar cells, Science 354 (2014) 542.

[3] J.M. Ball, M.M. Lee, A. Hey, H.J. Snaith, Low-temperature processed meso-superstructured to thin-film perovskite solar cells, Energy Environ. Sci. 6 (2013) 1739.

[4] B. Cai, Y. Xing, Z. Yang, W.H. Zhang, J. Qiu, High performance hybrid solar cells sensitized by organo-lead halide perovskites, Energy Environ. Sci. 6 (2013) 1480.

[5] Q. Wang, Y. Shao, Q. Dong, Z. Xiao, Y. Yuan, J. Huang, Large fill-factor bilayer iodine perovskite solar cells fabricated by a low-temperature solution-process, Energy Environ. Sci. 7 (2014) 2359.

[6] C. Zuo, L. Ding, An 80.11% FF record achieved for perovskite solar cells by using the NH_4Cl additive, Nanoscale 6 (2014) 9935.

[7] L. Etgar, P. Gao, Z. Xue, Q. Peng, A.K. Chandiran, B. Liu, M.K. Nazeeruddin, M. Grätzel, Mesoscopic $CH_3NH_3PbI_3/TiO_2$ heterojunction solar cells, J. Am. Chem. Soc. 134 (2012) 17396.

[8] M.M. Lee, J. Teuscher, T. Miyasaka, T.N. Murakami, H.J. Snaith, Efficient hybrid solar cells based on meso-super structured organometal halide perovskites, Science 338 (2012) 643.

[9] S. Wang, B. Liu, Y. Zhu, Z. Ma, B. Liu, X. Miao, R. Ma, C. Wang, Enhanced performance of TiO_2-based perovskite solar cells with Ru-doped TiO_2 electron transport layer, Sol. Energy 169 (2018) 335.

[10] W. Zhang, Y.-C. Wang, X. Li, C. Song, L. Wan, K. Usman, J. Fang, Recent advance in solution-processed organic interlayers for high-performance planar perovskite solar cells, Adv. Sci. 5 (2018) 1800159.

[11] a) S.S. Reddy, K. Gunasekar, J.H. Heo, S.H. Im, C.S. Kim, D.H. Kim, J.H. Moon, J. Y. Lee, M. Song, S.H. Jin, Highly efficient organic hole transporting materials for perovskite and organic solar cells with long-term stability, Adv. Mater. 28 (2016) 686;
b) S. S Reddy, S. Shin, U.K. Aryal, R. Nishikubo, A. Saeki, M. Song, S.-H. Jin, Highly efficient air-stable/hysteresis-free flexible inverted-type planar perovskite and organic solar cells employing a small molecular organic hole transporting material, Nanomater. Energy 41 (2017) 10.

[12] S.S. Reddy, V.M. Arivunithi, V.G. Sree, H. Kwon, J. Park, Y.C. Kang, H. Zhu, Y. Y. Noh, S.H. Jin, Lewis acid-base adduct-type organic hole transport material for high performance and air-stable perovskite solar cells, Nanomater. Energy 58 (2019) 284.

[13] S.K. Pathak, A. Abate, P. Ruckdeschel, B. Roose, K.C. Gödel, Y. Vaynzof, A. Santhala, S.-I. Watanabe, D.J. Hollman, N. Noel, A. Sepe, U. Wiesner, R. Friend, H.J. Snaith, U. Steiner, Performance and stability enhancement of dye-sensitized and perovskite solar cells by Al doping of TiO_2, Adv. Funct. Mater. 24 (2014) 6046.

[14] Y. Wang, D. Wu, L.-M. Fu, X.-C. Ai, D. Xu, J.-P. Zhang, Correlation between energy and spatial distribution of intragap trap states in the TiO_2 photoanode of dye-sensitized solar cells, ChemPhysChem 16 (2015) 2253.

[15] Y. Du, H. Cai, Y. Wu, Z. Xing, Z. Li, J. Xu, L. Huang, J. Ni, J. Li, J. Zhang, Enhanced planar perovskite solar cells with efficiency exceeding 16% via reducing the oxygen vacancy defect state in titanium oxide electrode, Phys. Chem. Chem. Phys. 19 (2017) 13679.

[16] a) J.K. Kim, S.U. Chai, Y. Ji, B. Levy-Wendt, S.H. Kim, Y. Yi, T.F. Heinz, J. K. Nørskov, J.H. Park, X. Zheng, Resolving hysteresis in perovskite solar cells with rapid flame-processed cobalt-doped TiO_2, Adv. Energy Mater. 8 (2018) 1801717;
b) L.F. Zhu, Y.Z. Xu, J.J. Shi, H.Y. Zhang, X. Xu, Y.H. Zhao, Y.H. Luo, Q.B. Meng, D.M. Li, Efficient perovskite solar cells via simple interfacial modification toward a mesoporous TiO_2 electron transportation layer, RSC Adv. 6 (2016) 82282.

[17] a) F. Giordano, A. Abate, J.P. Correa Baena, M. Saliba, T. Matsui, S.H. Im, S. M. Zakeeruddin, M.K. Nazeeruddin, A. Hagfeldt, M. Graetzel, Enhanced electronic properties in mesoporous TiO_2 via lithium doping for high-efficiency perovskite solar cells, Nat. Commun. 7 (2016) 10379;
b) B. Chen, M. Yang, S. Priya, K. Zhu, Origin of *J–V* hysteresis in perovskite solar cells, J. Phys. Chem. Lett. 7 (2016) 905.

[18] J. Peng, Y. Wu, Y. Wang, D. Jacobs, H. Shen, X. Fu, Y. Wan, T. Duong, N. Wu, C. Barugkin, H. Nguyen, D. Zhong, J. Li, T. Lu, Y. Liu, M.N. Lockrey, K. Weber, K. Catchpole, T. White, Interface passivation using ultrathin polymer-fullerene films for high-efficiency perovskite solar cells with negligible hysteresis, Energy Environ. Sci. 10 (2017) 1792–1800.

[19] H. Zhou, Q. Chen, G. Li, S. Luo, T.-b. Song, H.-S. Duan, Z. Hong, J. You, Y. Liu, Y. Yang, Interface engineering of highly efficient perovskite solar cells, Science 345 (2014) 542–546.

[20] L. Zuo, Z. Gu, T. Ye, W. Fu, G. Wu, H. Li, H. Chen, Enhanced photovoltaic performance of CH3NH3PbI3 perovskite solar cells through interfacial engineering using self-assembling monolayer, J. Am. Chem. Soc. 137 (2015) 2674–2679.

[21] K. Wojciechowski, S.D. Stranks, A. Abate, G. Sadoughi, A. Sadhanala, N. Kopidakis, G. Rumbles, C.-Z. Li, R.H. Friend, A.K.Y. Jen, H.J. Snaith, Heterojunction modification for highly efficient organic inorganic perovskite solar cells, ACS Nano 8 (2014) 12701–12709.

[22] Q. Guo, I. Cocks, E.M. Williams, The adsorption of benzoic acid on a TiO_2 (110) surface studied using STM, ESDIAD and LEED, Surf. Sci. 393 (1997) 1.

[23] J. Liu, Y. Wang, D. Sun, Enhancing the performance of dye-sensitized solar cells by benzoic acid modified TiO_2 nanorod electrode, J. Renew. Energy 38 (2012) 214–218.

[24] Y.S. Kwon, I.Y. Song, J.C. Lim, S.H. Park, A. Siva, T.H. Park, Reduced charge recombination by the formation of an interlayer using a novel dendron co adsorbent in solid-state dye-sensitized solar cells, RSC Adv. 2 (2012) 3467.

[25] J.M. Chiu, C.C. Chu, D.M. Zena, Y. Tai, Simultaneous enhancement of photocurrent and open circuit voltage in a ZnO based organic solar cell by mixed self-assembled monolayers, Appl. Energy 160 (2015) 681–686.

[26] a) Y.E. Ha, M.Y. Jo, J. Park, Y.-C. Kang, S.I. Yoo, J.H. Kim, Inverted type polymer solar cells with self-assembled monolayer treated ZnO, J. Phys. Chem. C 117 (2013) 2646;
b) Jone Emsley, The Elements, third ed., Clarendon Press, Oxford, 1998.

[27] X. Jiang, W. Zhang, S. Zhao, S. Zhou, Y. Shi, Z. Xin, Effect of benzoic acid surface modified alumina nanoparticles on the mechanical properties and crystallization behavior of isotactic polypropylene nanocomposites, RSC Adv. 8 (2018) 20790–20800.

[28] H.S. Wahab, Quantum chemical modeling study of adsorption of benzoic acid on anatase TiO_2 nanoparticles, J. Mol. Model. 18 (2012) 2709–2716.

[29] K.S. Kim, M.A. Barteau, Pathways for carboxylic acid decomposition on titania, Langmuir 4 (1988) 945–953.

[30] V.M. Arivunithi, S.S. Reddy, V.G. Sree, H.-Y. Park, J. Park, Y.-C. Kang, E.-S. Shin, Y.-Y. Noh, M. Song, S.-H. Jin, Efficiency exceeding 20% in perovskite solar cells with side-chain liquid crystalline polymer–doped perovskite absorbers, Adv. Energy Mater. 8 (2018) 1801637.

[31] Y. Shao, Z. Xiao, C. Bi, Y. Yuan, J.S. Huang, Origin and elimination of photocurrent hysteresis by fullerene passivation in CH 3 NH 3 PbI 3 planar heterojunction solar cells, Nat. Commun. 5 (2014) 5784.

[32] A. Campos, S. Riera-Galindo, J. Puigdollers, M. Mas-Torrent, Reduction of charge traps and stability enhancement in Solution Processed organic field-effect transistors based on a blended Ntype semiconductor, ACS Appl. Mater. Interfaces 10 (2018) 15952–15961.

[33] X. Xiao, C. Bao, Y. Fang, J. Dai, B.R. Ecker, C. Wang, Y. Lin, S. Tang, Y. Liu, Y. Deng Argon, Plasma treatment to tune perovskite surface composition for high efficiency solar cells and fast photodetectors, Adv. Mater. 30 (2018), 1705176.

[34] P. Liu, W. Wang, S. Liu, H. Yang, Z. Shao, Fundamental understanding of photocurrent hysteresis in perovskite solar cells, Adv. Energy Mater. 9 (2019) 180301713.

[35] A. Dualeh, T. Moehl, N. Tetreault, J. Teuscher, P. Gao, M.K. Nazeeruddin, M. Gratzel, Impedance spectroscopic analysis of lead iodide perovskite-sensitized solid-state solar cells, ACS Nano 8 (2014) 362.

[36] J.K. Kim, S.U. Chai, Y. Cho, L. Cai, S.J. Kim, S. Park, J.H. Park, X. Zheng, Ultrafast flame annealing of TiO_2 paste for fabricating dye-sensitized and perovskite solar cells with enhanced efficiency, Small 13 (2017) 1702260.

[37] X. Gu, Y. Wang, T. Zhang, D. Liu, R. Zhang, P. Zhang, J. Wu, Z.D. Chen, S. Li, Enhanced electronic transport in Fe^{3+}-doped TiO_2 for high efficiency perovskite solar cells, J. Mater. Chem. C 5 (2017) 10754.